Phase behavior of mixtures of hard ellipses: A scaled particle density functional study

Y. Martínez-Ratón

Grupo Interdisciplinar de Sistemas Complejos (GISC), Departamento de Matemáticas,

Escuela Politécnica Superior, Universidad Carlos III de Madrid,

Avenida de la Universidad 30, E-28911, Leganés, Madrid, Spain

Abstract

We present a scaled particle density functional study of two-dimensional binary mixtures of hard convex particles with one or both species being ellipses. In particular, we divide our study into two parts. The first part is devoted to the calculation of phase diagrams of mixtures with the same elliptical shapes, but with (i) different aspect ratios and equal particle areas, (ii) equal aspect ratios and different particle areas and (iii) with the former and the later being different. In the second study we obtain the phase diagrams corresponding to crossed-mixtures of particles with species having elliptical and rectangular shapes. We compare the phase diagram topologies and explain their main features from the entropic nature of particle interactions directly related to the anisotropies, areas, and shapes of species. The results obtained can be corroborated by experiments on granular rods where the entropic forces are very important in the stabilization of liquid-crystal textures at the stationary states.

I. INTRODUCTION

The demixing transition in mixtures of hard convex three-dimensional particles have received a considerably attention from the theoretical point of view [1–14]. This is due to the possibility of formulating relatively simple theoretical models for mixtures of anisotropic particles which are not allowed to overlap. These models are based on the simple Onsager second-virial approximation [15] or its rescaled version, the Parsons approach [16]. Also, the scaled particle theory (SPT), proposed firstly for hard spheres [17] and later extended to other particles geometries [18–22], has been a fruitful theoretical tool in the study of these kind of mixtures. All these models predict that a binary mixture of asymmetric enough particles can demix into two different phases, each one rich in different species. The nature of uniform demixed phases can be isotropic (I), a fluid with randomly oriented particle axis, or nematic (N) in which the particles' axes are oriented in average along the nematic director. All possible demixing transitions, i.e. I-I, N-N and I-N were found from the numerical implementation of these models.

In two dimensions the theoretical works devoted to the study of the demixing transitions are more scarce, because strictly two-dimensional fluids occur less often in nature compared to the three-dimensional fluids. Examples of the former constitute the quasi-two-dimensional films obtained from preferential chemical adsorption of certain species at interfaces. The adsorption of polystyrene spheres [23] or ellipsoidal latex particles [24] into a two-dimensional interface has allowed the experimental study of freezing and percolation/jamming transitions in two dimensions respectively. Also, the time-dependent behavior of anisotropic colloids near interfaces was recently studied through a theoretical modelling of the Langevin dynamics of adsorbed particles at a flat interface [25]. For a recent review on the behavior of colloidal particles at liquid interfaces see Ref. [26].

However, the most paradigmatic example constitutes the collection of granular anisotropic particles confined between two parallel plates with the distance between them less than the particle widths. A growing number of experimental works conducted on granular fluids subjected to different vibrational modes show spatial pattern formations, demixing scenarios of granular species and collective motions [27]. Those systems in which granular rods are vertically shacked have shown that the entropic nature of interactions between particles is very important in the explanation of phenomenology found. In particular, the presence of

defects of the nematic director due to the difference between particle orientations near and far from the walls was found [28]. Recent experiments on granular rods reported the presence of certain liquid-crystal textures with N, tetratic (T), and smectic (Sm) symmetries as the stationary states of these systems [29]. The presence of strong dissipation due to the inelastic interactions between grains is an important ingredient to take into account in any theoretical model of a shaken granular systems. However, the presence of demixed stationary states of a granular mixture could be described by models based of density functional theory. For example the ranges of molar and packing fractions for which the demixing is observed could be approximately given by these models.

The SPT shows that a two-dimensional mixture of hard convex bodies never demixes into two I phases [30]. However, recently we have shown that the same theory can predict I-N and N-N demixing [31, 32]. The only difference with respect to three dimensions is the second order character of the I-N transition at pressures bellow the tricritical point [31, 32]. The main purpose of the present study is to implement the SPT for (i) a mixture of hard ellipses (HEs) with different aspect ratios and/or particle areas and (ii) for crossed-mixtures composed of HEs and hard rectangles (HR). The most convex particle with a fixed aspect ratio that can be imagined in two dimensions is just an ellipse. This property in turn might be reflected in the phase behavior of mixtures composed of HEs. We will show that this is indeed the case by studying the phase diagram topology as a function of particle aspect ratio and particle area. The one-component fluid of HEs has been studied via Monte Carlo simulations. This fluid exhibits, for high enough aspect ratios, an I-N transition occurring via the disclination unbinding mechanism, while for higher packing fractions a first order fluid-solid transition takes place [33]. It has been shown that the equation of state for the one-component fluid of HEs following the SPT compares reasonable well with the simulation results |34|.

To implement the present study we firstly find an analytical expression for the excluded area between two HEs with different axes $\{a_i, b_i\}$ (i = 1, 2). Zheng and Palffy-Muhoray [35] developed a method based on the calculation of the distance of closest approach between an ellipse and a circle. Thus, after rescaling the circle they obtained the distance of closest approach between two ellipses. Finally, the excluded area can be obtained by the angular integration of the distance of closest approach. However, this integral should be evaluated numerically. We will follow another procedure, in which the excluded area between two dif-

ferent ellipses can be calculated from the parametrization of the distance of closest approach as a function of the angle that forms the point of contact between two ellipses with a fixed reference axis. The resulting excluded area thus depends on the complete elliptic integral with its parameter being a function of the ellipse eccentricities and on the relative angle between particles. Further, we also calculate the excluded area between an ellipse and a rectangle. The details of both calculations are relegated to the appendices.

This paper is organized as follows. In Sec. II we present the theoretical model used for the present study: the SPT. In Sec. III we analytically derive the spinodal curves of the I-N second-order transition, i.e. the packing fraction as a function of composition for general mixtures of two-dimensional hard particles. Sec. IV is devoted to the analytical derivation of the N-N spinodal curve with the constraint of parallel particle alignment. In Sec. V we present the phase diagrams of mixtures of HEs (Sec. VA) and HEs and HRs (Sec. VB) obtained from the numerical minimization of the free-energy functional. Finally, in Sec. VI the main conclusions are drawn. The appendices contain the details of the derivation of the excluded area between two HEs (Sec. A) and HEs and HRs (Sec. B) and different mathematical aspects of the functional minimization procedure (Sec. C).

II. SCALED PARTICLE THEORY

The central quantity of any theoretical model which accounts for two-dimensional hard particle interactions is the pair excluded area to particle ν due to the presence of particle μ with the constraint of a fixed angle ϕ between their main axis. Because the hard core nature of interactions, both particles can not overlap and thus the excluded area $A_{\mu\nu}(\phi)$ defines a body with a geometry directly related with those of particles. The present paper is devoted to the study of phase diagrams of mixtures composed of HEs with different characteristic lengths [different semi-axis (a_{μ}, b_{μ})] and a crossed–mixture of HEs and HRs. In Appendices A and B we obtain the analytical formulas for the excluded areas of these mixtures. Once the excluded area is given we can construct a scaled particle theory (SPT) for a general mixture [17]. The excess free energy per particle following the SPT can be calculated to be

$$\varphi_{\rm ex} = -\ln(1-\eta) + \frac{\rho}{1-\eta} \sum_{\mu\nu} x_{\mu} x_{\nu} \langle \langle A_{\mu\nu}^{(0)} \rangle \rangle, \tag{1}$$

where ρ is the total number density and $\eta = \rho \sum_i x_i a_i$ is the total packing fraction with x_i the molar fraction of species i and a_i their particle areas. We have defined the function $A_{\mu\nu}^{(0)}(\phi) = (A_{\mu\nu}(\phi) - a_{\mu} - a_{\nu})/2$, and used the short-hand notation

$$\langle \langle A_{\mu\nu}^{(0)} \rangle \rangle = \int_0^{\pi} d\phi_1 \, h_{\mu}(\phi) \int_0^{\pi} d\phi_2 \, h_{\nu}(\phi) A_{\mu\nu}^{(0)}(\phi_1 - \phi_2), \tag{2}$$

to define the double angular average of $A_{\mu\nu}^{(0)}(\phi)$ with respect to the orientational distribution functions $h_{\mu}(\phi)$. Note that the second order density expansion of Equation (1) give us the usual second virial approximation

$$\varphi_{\text{ex}}^{(b_2)} = \frac{\rho}{2} \sum_{\mu\nu} x_{\mu} x_{\nu} \langle \langle A_{\mu\nu} \rangle \rangle. \tag{3}$$

The fact that the coefficients $\langle\langle A_{\mu\nu}^{(0)}\rangle\rangle$, instead of the excluded areas, enter into the SPT free-energy is due to the form of the derived SPT: through a Taylor expansion of the excess chemical potential corresponding to the scaled particle, evaluated at low densities. The upper limit of integration in Equation (2) is π due to the head-tail symmetry of particles, i.e. $h_{\mu}(\phi) = h_{\mu}(\pi - \phi)$. These functions measure the degree of orientation of the particles along the fixed nematic director. In the present paper we have selected a variational family for these functions as

$$h_{\mu}(\phi) = \frac{\exp\left(\lambda_{\mu}\cos 2\phi\right)}{\pi I_0(\lambda_{\mu})},\tag{4}$$

with $I_n(x)$ the n-th order modified Bessel function. The perfect nematic alignment is reached when $\lambda_{\mu} \to \infty$, which gives us $h_{\mu}(\phi) = \delta(\phi)$ (the Dirac-delta function), while the isotropic fluid is obtained in the limit $\lambda_{\mu} \to 0$ for which $h_{\mu}(\phi) = \pi^{-1}$. Note that this parametrisation excludes the possibility of study of the tetratic phase with fourfold angular symmetry $h_{\mu}(\phi + \pi/2) = h_{\mu}(\phi)$.

The ideal part of the free-energy per particle can be computed as

$$\varphi_{\rm id} = \ln \eta - 1 + \sum_{\mu} x_{\mu} \left\{ \ln x_{\mu} + \int_{0}^{\pi} d\phi h_{\mu}(\phi) \ln \left[\pi h_{\mu}(\phi) \right] \right\},$$
(5)

$$= \ln \eta - 1 + \sum_{\mu} x_{\mu} \left\{ \ln x_{\mu} + \lambda_{\mu} \frac{I_{1}(\lambda_{\mu})}{I_{0}(\lambda_{\mu})} - \ln I_{0}(\lambda_{\mu}) \right\}.$$
 (6)

where we have inserted (4) into (5) to obtain (6).

The Gibbs free energy per particle $g = \varphi + P/\rho$ (with $\varphi = \varphi_{id} + \varphi_{exc}$ the total free-energy per particle) calculated at a constant fluid pressure P should be minimized with respect

to the parameters λ_{μ} ($\mu = 1, 2$) to obtain their equilibrium values. The expression for the pressure following the SPT is

$$\beta P = \frac{\rho}{1-\eta} + \frac{\rho^2}{(1-\eta)^2} \sum_{\mu\nu} x_{\mu} x_{\nu} \langle \langle A_{\mu\nu}^{(0)} \rangle \rangle. \tag{7}$$

In Appendix C we write explicit expressions for the equations to be solved numerically to obtain the equilibrium values of λ_{μ} . The common tangent construction of the function g(x), with $x = x_1$, allows us to calculate the coexisting values for x (and thus of η once the fluid pressure is fixed) at the demixing transition.

III. I-N BIFURCATION ANALYSIS

In this section we obtain an analytic expression for the I-N spinodal of a general mixture. When $\lambda_{\mu} \ll 1$ we can approximate the orientational distribution functions $h_{\mu}(\phi)$ up to first order in λ_{μ} by

$$h_{\mu}(\phi) = \frac{1}{\pi} \left(1 + \lambda_{\mu} \cos 2\phi \right). \tag{8}$$

Inserting this expression in the free-energy per particle $\varphi = \varphi_{id} + \varphi_{exc}$ we obtain, up to second order in λ_{μ}

$$\varphi = \frac{1}{4} \sum_{\mu} x_{\mu} \lambda_{\mu}^{2} + \frac{y}{2} \sum_{\mu\nu} x_{\mu} x_{\nu} \left[\alpha_{\mu\nu}^{(0)} + \alpha_{\mu\nu}^{(1)} \lambda_{\mu} \lambda_{\nu} \right], \tag{9}$$

with $y = \rho/(1-\eta)$ and where we have defined the coefficients

$$\alpha_{\mu\nu}^{(i)} = \frac{1}{\pi} \int_0^{\pi} d\phi \cos(2i\phi) A_{\mu\nu}^{(0)}(\phi), \quad i = 0, 1.$$
 (10)

The minimization of (9) with respect to λ_{μ} give us

$$\frac{\partial \varphi}{\partial \lambda_{\mu}} = \frac{x_{\mu}}{2} \left[\lambda_{\mu} + 2y \sum_{\nu} \alpha_{\mu\nu}^{(1)} x_{\nu} \lambda_{\nu} \right] = 0. \tag{11}$$

The term of Eq. (11) enclosed by square brackets can be put in the following matrix form

$$H\lambda \equiv (I + 2yU)\lambda = 0, \tag{12}$$

where $\lambda \equiv (\lambda_1, \lambda_2)^T \neq \mathbf{0}$, I is the 2×2 identity matrix while U is the matrix with elements $\alpha_{\mu\nu}^{(1)} x_{\nu}$. Equation (12) has a nontrivial solution only if $\det(\mathbf{H}) = 0$, which gives us the following result:

$$1 + 2y\tau + (2y)^2 x_1 x_2 \left\{ \alpha_{11}^{(1)} \alpha_{22}^{(1)} - \left[\alpha_{12}^{(1)} \right]^2 \right\} = 0, \tag{13}$$

where we have defined the coefficient

$$\tau = \sum_{\mu} x_{\mu} \alpha_{\mu\mu}^{(1)}. \tag{14}$$

Taking into account that the expression enclosed by brackets in Equation (13) is equal to zero for any mixture of convex bodies, we find that the packing fraction at the I-N transition can be calculated as

$$\eta^* = \frac{y^* \langle a \rangle}{1 + y^* \langle a \rangle}, \quad y^* = -\frac{1}{2\tau}, \tag{15}$$

where we have used the shorthand notation $\langle a \rangle = \sum_{\mu} x_{\mu} a_{\mu}$. Following the SPT the pressure of the isotropic fluid at the bifurcation point can be calculated as

$$\beta P^* = y^* \left\{ 1 + \frac{1}{4\pi} y^* \left[\sum_{\mu} x_{\mu} \mathcal{L}_{\mu} \right]^2 \right\},$$
 (16)

where \mathcal{L}_{μ} is the perimeter of species μ .

IV. N-N DEMIXING

In this section we obtain analytically the criterion for the existence of N-N demixing and its spinodal curve with the constraint of parallel particle alignment. This constraint is necessary to obtain an explicit analytic function for this spinodal, while the freely rotating case can only be solved numerically. The spinodal instability of the binary mixture with respect to phase separation can be computed by requiring that $\mathcal{H}(\eta, x) = 0$ where we have defined

$$\mathcal{H}(\eta, x) \equiv \left[1 + \rho_1 \frac{\partial^2 \Phi}{\partial \rho_1^2} \right] \left[1 + \rho_2 \frac{\partial^2 \Phi}{\partial \rho_2^2} \right] - \rho_1 \rho_2 \left[\frac{\partial^2 \Phi}{\partial \rho_1 \partial \rho_2} \right]^2, \tag{17}$$

with $\rho_i = x_i \rho$, while $\Phi = \rho \varphi_{\text{ex}}$ is the excess part of the free energy density. From Equations (1) and (17) we obtain

$$\mathcal{H}(\eta, x) = (1 + y_0)^2 \left\{ 1 + 2y_0 - 4x(1 - x)y_0^2 \mathcal{U} \right\}, \tag{18}$$

where we have defined $y_0 = \eta/(1-\eta)$, and $\mathcal{U} = (q^2-1) a_1 a_2/\langle a \rangle^2$, with $q = A_{12}^{(0)}/\sqrt{a_1 a_2}$. Solving $\mathcal{H}(\eta, x) = 0$ for η , we find the explicit expression

$$\eta = \frac{1}{\sqrt{1 + 4x(1 - x)\mathcal{U}}}.\tag{19}$$

The packing fraction and composition at the critical point are $\eta^* = 1/q$, and $x^* = a_2/(a_1 + a_2)$, respectively. Finally, the pressure at this point is

$$\beta P^* a_2 = q \left[\frac{1 + \sqrt{a_2/a_1}}{q - 1} \right]^2. \tag{20}$$

We conclude that demixing transition occurs only if U > 0, i.e. for q > 1. For mixtures of HEs we find $q_{ee} = 2\sqrt{s}E\left[1 - s^{-2}\right]/\pi \ge 1$, where we have defined the coefficient

$$s = \kappa_2/\kappa_1 \ge 1,\tag{21}$$

with κ_i the aspect ratio of particle i while E[x] is the complete elliptic integral of the second kind. The same coefficients for a mixture of HRs and for a crossed-mixture of HEs and HRs are $q_{\rm rr} = (\sqrt{s} + 1/\sqrt{s})/2 \ge 1$ and $q_{\rm er} = (\sqrt{s} + 1/\sqrt{s})/\sqrt{\pi} \ge 2/\sqrt{\pi} > 1$ respectively. We see that for s = 1 (no matter what the ratio a_2/a_1 is) no demixing occurs in mixtures of particles with the same shape, while the crossed-mixture demixes even in this case. In Figure 1 we plot the coefficients $q_{\alpha\beta}$ as a function of s. It is interesting to note that at $s \approx 5.759$ two of the curves intersect (those corresponding to the mixture of HEs and the crossed-mixture). To illustrate the effect of this cross-over on the phase behavior we plot in Figure 2 the spinodals of both types of mixtures for s = 2.5 and s = 8, which are located at different sides of the cross-over point.

V. RESULTS

All the phase diagrams we present in this section were calculated via the bifurcation analysis (see Section III) for the case of continuous phase transitions (as the second order I-N transition) and from the numerical minimisation of the parametrised Gibbs free energy per particle (see Section II and Appendix C) for the case of I-N or N-N demixing transitions. The later procedure allows us to obtain the equilibrium orientational distribution functions $h_{\mu}(\phi)$ at coexistence and the coexisting values of the composition and packing fraction of the demixed phases at a given pressure. We begin the presentation of the results from the most simple binary mixture: a mixture of HEs. Note that the hard disk (HD) is a special case of ellipse with equal semi-axis.

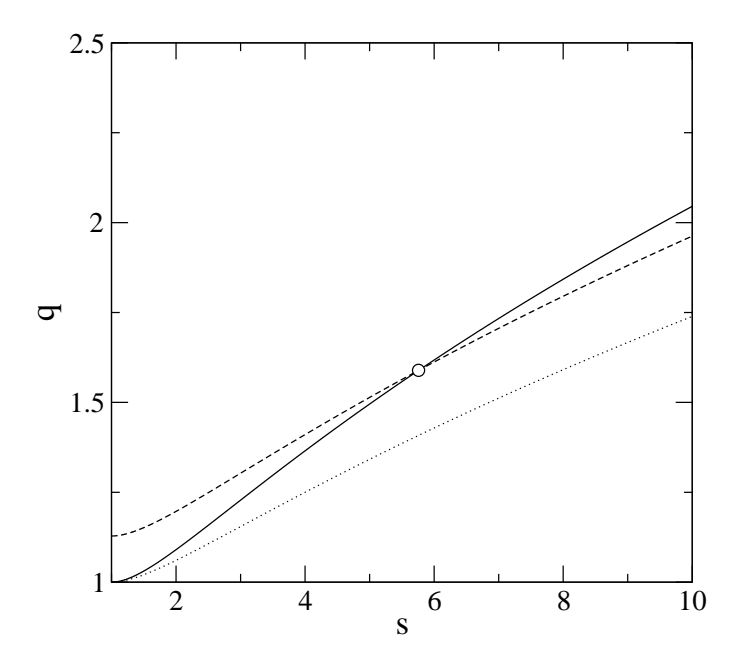


FIG. 1: The coefficient q as a function of $s = \kappa_2/\kappa_1$ for a mixture of HEs (solid curve), for the crossed-mixture of HEs and HRs (dashed curve), and for a mixture of HRs (dotted curve). The open circle shows the cross-over point.

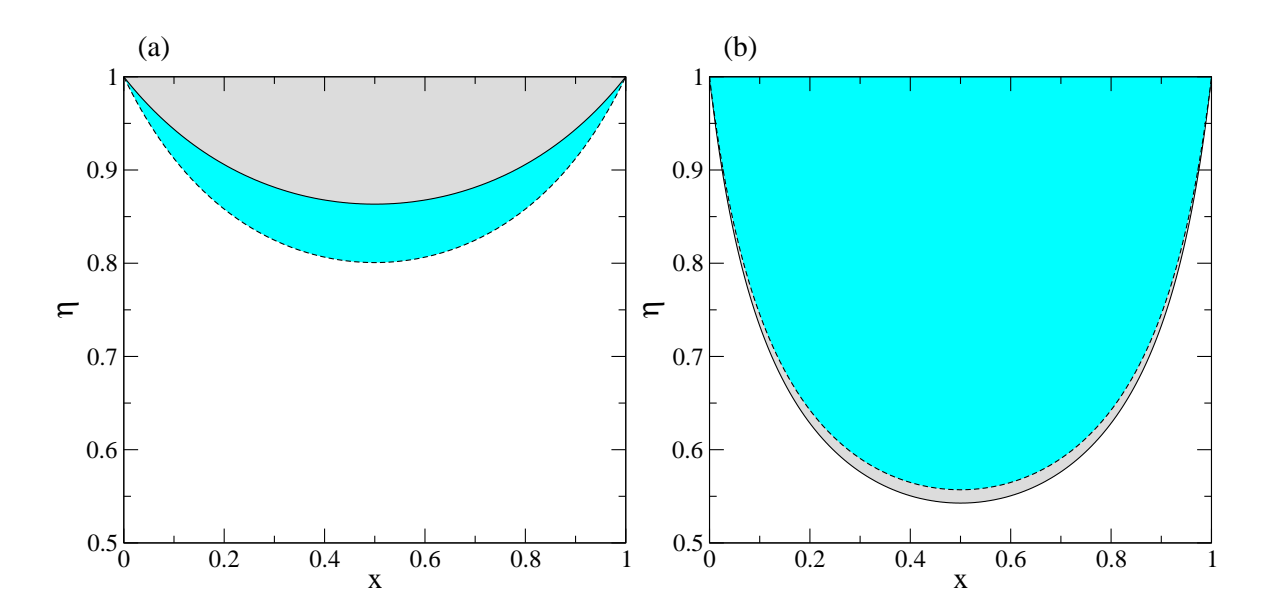


FIG. 2: Demixing spinodals of mixtures of HEs (solid line) and of the crossed-mixture of HEs and HRs (dashed line) for s=2.5 (a) and s=8 (b).

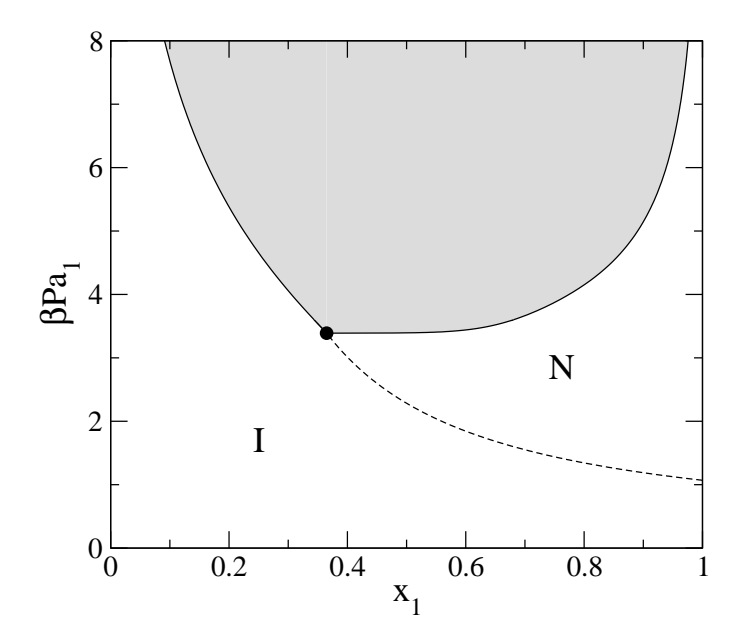


FIG. 3: Phase diagram of the binary mixture of HEs (species 1) with $\kappa_1 = 10$ and HDs (species 2). Both species have the same particle areas $a_1 = a_2$. The regions of I and N stability are correspondingly labeled. The I-N spinodal is plotted with dashed line while the demixing binodals are shown with solid lines. The grey region constitutes the zone of mixture instability. The tricritical point is shown with a filled circle.

A. Mixtures of HE

The phase diagram topologies we show here are similar to those obtained for mixtures of HRs and hard discorectangles (HDRs) in recent studies [31, 32]. These studies have shown all possible demixing scenarios that mixtures of two-dimensional hard convex particles can exhibit. However, we will show that the ellipse, being the geometry with the most convex anisotropy we can imagine, considerably enhance the demixing transition in mixtures of particles with elliptical shapes.

The first binary mixture we study is composed of HEs and HDs. The former has an aspect ratio of $\kappa_1 = 10$ while the area of both species are the same $(a_1 = a_2)$. The resulting phase diagram is shown in Figure 3 as a pressure—HE molar fraction (x_1) plot. As we can see from this figure, at low pressures the mixture exhibits a second order I-N phase transition up to pressure value of $\beta Pa_1 \approx 3.7$ (the location of a tricritical point) above which the system demixes into an I phase rich in HDs and a N phase rich in HEs. The demixing gap is wider as

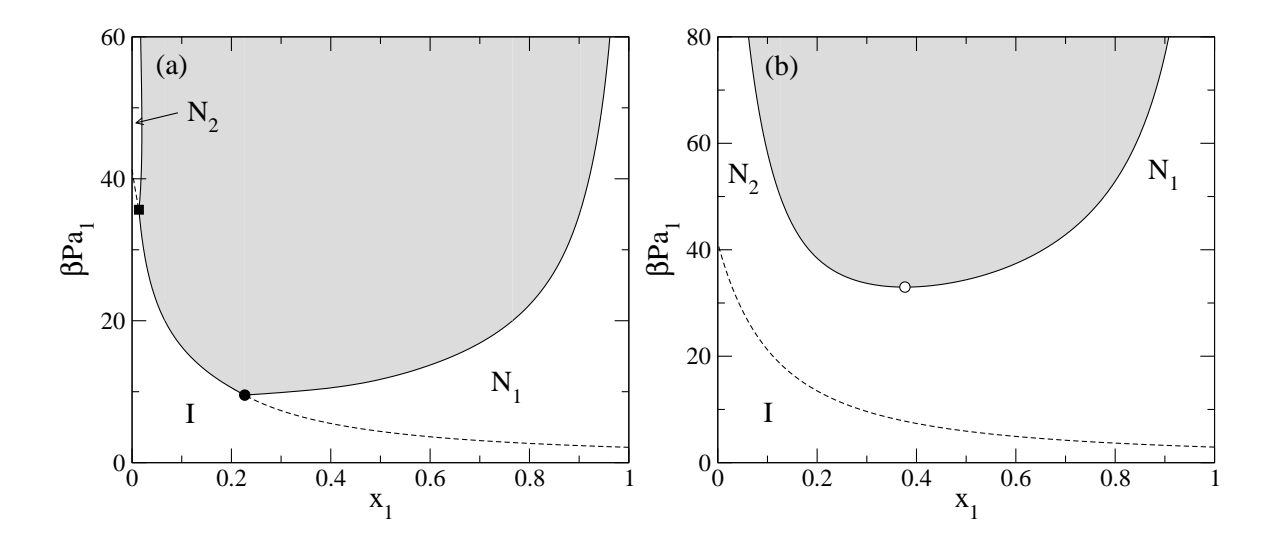


FIG. 4: Phase diagram of two binary mixtures of HEs with $(\kappa_1, \kappa_2) = (6, 2)$ (a) and $(\kappa_1, \kappa_2) = (5, 2)$ (b) while the particles areas of both species are equals. The meanings of different lines and labels coincide with those of Fig. 3. The tricritical and critical endpoints are shown with filled circle and square, respectively. Finally, the critical point is shown with an open circle.

the pressure increases from the tricritical point. We should point out that the second order I-N transition obtained from density functional calculations replace the Kosterlitz-Thouless I-N transition obtained by simulations and theoretical models that properly account for the nematic director fluctuations. The SPT theory does not includes these fluctuations, thus predicting a continuous increase of the long range nematic ordering.

The second study we have carried out concerns the calculation of the phase diagram of two similar binary mixtures of HEs, again with the same particle area $a_1 = a_2$ but with different aspect ratios given by $\kappa_1 = 6$ and $\kappa_2 = 2$ for the first mixture [Figure 4 (a)] while they are $\kappa_1 = 5$ and $\kappa_2 = 2$ for the second mixture [Figure 4 (b)]. There is an important difference between both phase diagrams in that the first one has a region of I-N demixing above the tricritical point [see Figure 4 (a)] which is replaced at higher pressures by a N-N demixing (just when the I-N spinodal intersects the I binodal of the I-N coexistence). We call this point a critical end point. The I phase as usual is rich in HE species with small aspect ratio. The second phase diagram exhibits a second order I-N transition for all compositions and at higher pressures the system demix into two different N phases. This N-N demixing transition ends at a critical point.

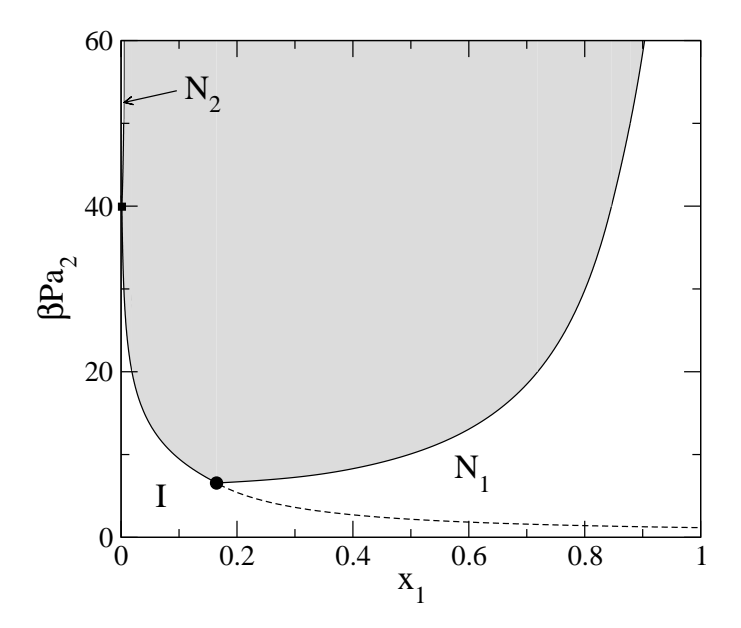


FIG. 5: Phase diagram of a binary mixture of HEs with aspect ratios $\kappa_1 = 5$ and $\kappa_2 = 2$ while the partcle area $a_1 = 2.5a_2$. The meanings of labels and lines are as in Figigure 3.

How affects the difference in particle areas on the phase behavior constitutes the following point we have elucidated. The aspect ratios of both ellipses are again $\kappa_1 = 5$ and $\kappa_2 = 2$ while the ratio between particle areas is $a_1/a_2 = 2.5$. In Fig. 5 we show the resulting phase diagram. Again appears a window of I-N demixing but now the stability region of the second nematic (N₂) shrinks considerably.

Now we consider a mixture of HEs with the same aspect ratios $\kappa_1 = \kappa_2 = 5$ and different areas, specifically $a_1/a_2 = 50$. The phase diagram is shown in Figure 6. This mixture exhibits two tricritical points defining the lower and upper limits of the I-N demixing and two critical points defining the proper limits of the N-N phase separation. In Figure 6 the molar fraction of the first species is substituted by its area fraction, i.e. $x_a = x_1 a_1/(x_1 a_1 + x_2 a_2)$. In such a way the position of all these points can be properly discerned.

B. Mixtures of HE and HR

This section is devoted to the study of mixtures of particles with different shapes, specifically HE- and HR-shaped particles. The first crossed-mixture we have studied is composed of species with aspect ratios coinciding with those of the already studied HE mixture with

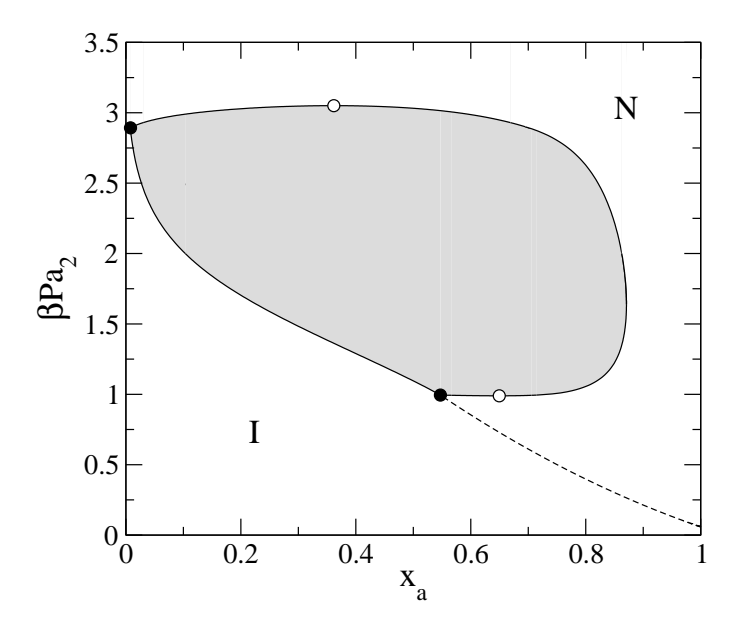


FIG. 6: Mixture of HEs with the same aspect ratios $\kappa_1 = \kappa_2 = 5$ and different particle areas $a_1 = 50a_2$. The critical and tricritical points are shown with open and filled circles respectively.

phase diagram plotted in Figure 4 (b). Specifically the HR has the larger aspect ratio ($\kappa_1 = 5$) while the HE has $\kappa_2 = 2$, and the areas of booth particles coincide. The aspect ratio of the rectangular particles is selected so as to be large enough to forbid the T phase stability [31]. In Figure 7 we show the phase diagram of this mixture. In the same figure we plot for a better comparison the phase diagram of Figure 4 (b). We can extract two main differences between both phase diagrams. Firstly, the I-N transition occurs at lower pressures for the HE mixture. This feature is related to the change in the excluded area as the particle aligns preferentially along the nematic director. This change is larger in mixtures of HEs compared with crossed-mixtures. The other main difference is related to the size of the N-N demixing gap. The crossed-mixture has the wider gap which can be understood in terms of packing of particles at high pressures: particles with the same shape pack better than those with different shapes. This in turn has already been quantified in Section IV through the coefficients q_{ee} and q_{er} (see Figure 1).

The last study we have carried out is related to the effect that different particle shapes have on the phase diagrams of binary mixtures with species having very dissimilar areas (specifically $a_1 = 50a_2$) but equal aspect ratios (which were fixed to 5). To this purpose we have calculated the phase diagrams of a mixture of HEs (the dotted lines in Figure 8), a

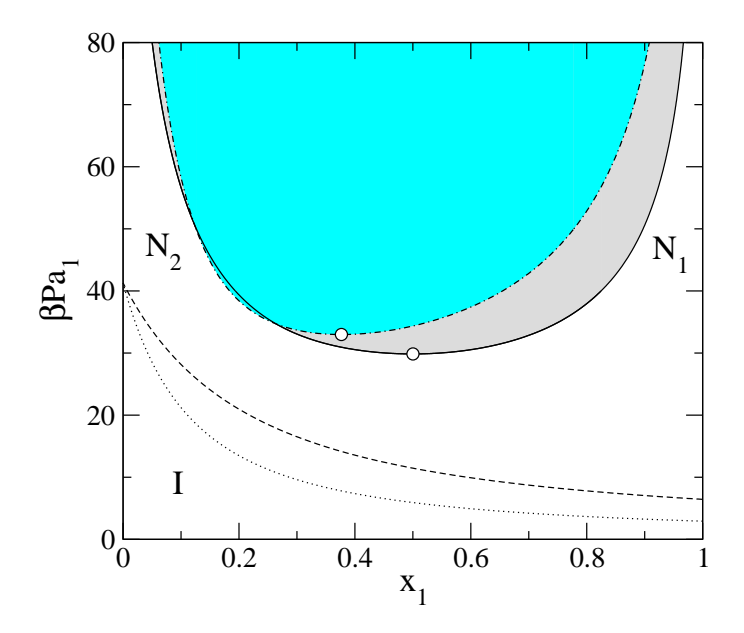


FIG. 7: A mixture of HRs (species 1) and HEs (species 2) with the same particle areas $a_1 = a_2$ while the aspect ratios are $\kappa_1 = 5$ and $\kappa_2 = 2$, respectively. The dashed line represents the I-N spinodal while the solid lines represent the N₁-N₂ demixing transition. Also plotted is the phase diagram of Figure 4 (b) corresponding to the mixture of HEs with the same particle aspect ratios and areas. The dotted and dashed-dotted lines represent the spinodal and demixing curves, respectively, for this case.

crossed—mixture of HEis and HRs with rectangles being the large species (the solid line in Figure 8) and the opposite mixture with the ellipses being the large species (the dot-dashed line in Figure 8). As we can see from this figure the lower I-N spinodal corresponds to the mixture of HEs which is related to the major gain in the excluded area by the particle alignment of the most convex species, the HEs. For the same reason, we expect that the I-N demixing region is widened for crossed-mixtures with ellipses being the large species. The mixture of HEs and HRs, the later being the large species, has the smallest demixing gap which is related to the fact that a great amount of large rectangles enhances the stability of the isotropic phase with respect to the nematic, due to the disordered effect that cause the rectangular corners. Finally, the scenario with an intermediate demixing gap occurs for mixtures of HEs.

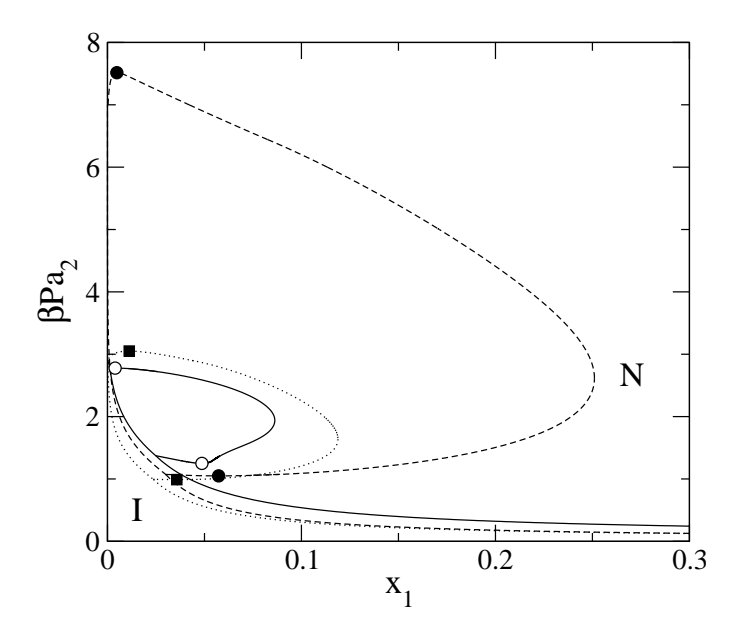


FIG. 8: Phase diagrams of the binary mixtures with equal particle aspect ratios ($\kappa_1 = \kappa_2 = 5$) but different areas ($a_1 = 50a_2$). The dotted lines represent the mixture of HEs, the solid lines represent the mixture of HRs (species 1) and HEs (species 2) and the dot-dashed lines represent the mixture of HEs (species 1) and HRs (species 2). The positions of critical points are shown with different symbols.

VI. CONCLUSIONS

One of the main purposes of the present work has been to encourage the statistical mechanical study of two-dimensional mixtures of hard anisotropic particles as a starting point to understand the phenomenology inherent in mixtures of granular particles. While three-dimensional mixtures have been systematically studied via density functional calculations and by MC simulations, there is a lack of results on two-dimensional mixtures, with scarce theoretical works and no simulation results.

We have shown here that the phenomenology inherent to these mixtures are as rich as the three-dimensional mixtures, with all possible demixing scenarios where the demixed phases have isotropic or nematic symmetries. The absence of I-I demixing and the presence of second order I-N transition constitute the main differences with respect to the three-dimensional case.

While mixtures of hard particles with rectangular and disco-rectangular geometries have

been recently studied with density functional tools [31, 32], the present work constitutes the first attempt to incorporate the elliptical geometry into these studies. For a given aspect ratio the ellipse is the most convex particle we can imagine. As we have shown here, this geometrical property is translated to the phase diagram topologies of mixtures with one or both species being ellipses. We trust that the same kind of results can be found in mixtures of ellipsoidal and cylindrical granular rods, the Basmati rice being an important paradigm of the former.

We should take the conclusions about the stability of uniform phases that the SPT predicts with certain caution. Phase transitions to non-uniform phases, such as smectic or crystalline phases, can occur at pressures bellow the maximum values depicted in the phase diagrams plotted here. Only a full minimization of a density functional with respect to the density profile $\rho(\mathbf{r}, \phi)$ (depending also on the spatial variables) can clarify this problem. A density functional for mixtures of HEs based on the Parsons approach can in principle be implemented for the general density profile inhomogeneities. However this functional treats the translational degrees of freedoms in a crude approximation, wich is a serious drawback for two-dimensional systems where the many-body correlations are very important.

Acknowledgments

This work is part of the research project MOSAICO and we acknowledge support from grant FIS2010-22047-C05-C04 from the Ministerio de Ciencia y Tecnología, and grant MODELICO-CM from Comunidad Autónoma de Madrid (Spain).

Appendix A: Calculation of the excluded area between two ellipses

In this section we calculate the excluded area between two different ellipses. The center of an ellipse with semi-axis \mathbf{a}_1 and \mathbf{b}_1 will be placed at the origin of the coordinate system with the major semi-axis \mathbf{b}_1 being parallel to the y Cartesian axis. The other ellipse, with semi-axes \mathbf{a}_2 , \mathbf{b}_2 , is placed at the point $\mathbf{r}_0 = (x_0, y_0)$ and has its major axis forming and angle ϕ with respect to the long axis of the first ellipse. The vector \mathbf{r}_0 is such that there is only one common tangent point between both ellipses (see Figure 9).

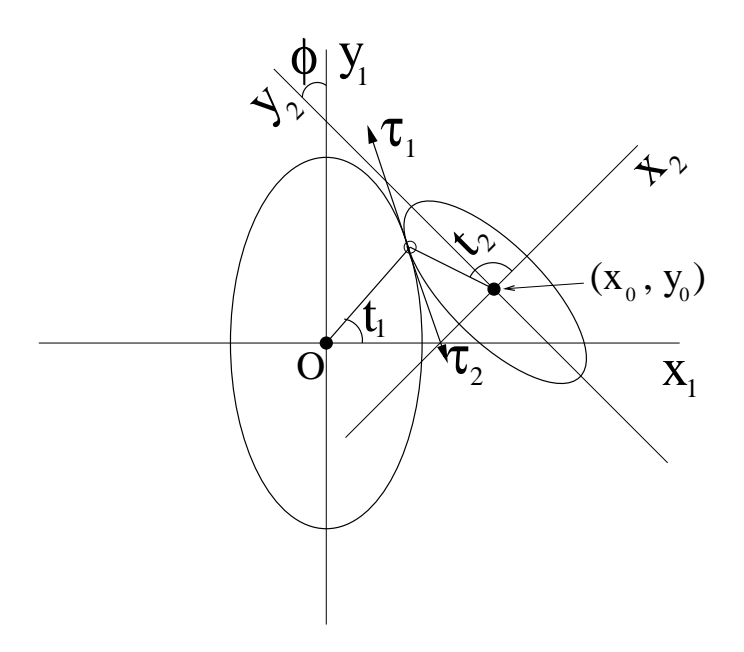


FIG. 9: Configuration of the closest approach between two ellipses with semi-axes $\{a_1, b_1\}$ and $\{a_2, b_2\}$ with a relative orientation defined by the angle between their long axis, which is equal to ϕ .

The parametrised coordinates of the first ellipse are

$$\mathbf{r}_1(t_1) = [x_1(t_1), y_1(t_1)] = (\mathsf{a}_1 \cos t_1, \mathsf{b}_1 \sin t_1), \quad t_1 \in [0, 2\pi], \tag{A1}$$

while the second vector $\mathbf{r}_2(t_2) = [x_2(t_2), y_2(t_2)]$ is parametrically defined as

$$x_2(t_2) = x_0 + \mathsf{a}_2 \cos t_2 \cos \phi - \mathsf{b}_2 \sin t_2 \sin \phi,$$
 (A2)

$$y_2(t_2) = y_0 + b_2 \sin t_2 \cos \phi + a_2 \cos t_2 \sin \phi$$
 (A3)

with $t_2 \in [0, 2\pi]$. The tangent unit vectors $\boldsymbol{\tau}_i$ corresponding to both ellipses, calculated by differentiating $[x_i(t_i), y_i(t_i)]$ with respect to the parameters t_i , are

$$\tau_1(t_1) = \frac{1}{\tau_1}(-\mathsf{a}_1 \sin t_1, \mathsf{b}_1 \cos t_1), \tag{A4}$$

$$\boldsymbol{\tau}_2(t_2) = \frac{1}{\tau_2} (-\mathsf{a}_2 \sin t_2 \cos \phi - \mathsf{b}_2 \cos t_2 \sin \phi, \mathsf{b}_2 \cos t_2 \cos \phi - \mathsf{a}_2 \sin t_2 \sin \phi), \tag{A5}$$

where $\tau_i = \sqrt{\mathsf{a}_i^2 \sin^2 t_i + \mathsf{b}_i^2 \cos^2 t_i}$. The condition of a common tangent point between both ellipses can be expressed by the following set of equations:

$$\mathbf{r}_1(t_1) = \mathbf{r}_2(t_2), \tag{A6}$$

$$\boldsymbol{\tau}_1(t_1) = -\boldsymbol{\tau}_2(t_2), \tag{A7}$$

which can be solved to obtain $\sin t_2$ (or $\cos t_2$) as a function of t_1 and also for $x_0(t_1)$ and $y_0(t_1)$ with the result

$$\sin t_2 = \frac{\mathsf{b}_2(\mathsf{b}_1 \cos t_1 \sin \phi - \mathsf{a}_1 \sin t_1 \cos \phi)}{\delta(t_1)^{1/2}},\tag{A8}$$

$$\cos t_2 = \frac{-\mathsf{a}_2(\mathsf{a}_1 \sin t_1 \sin \phi + \mathsf{b}_1 \cos t_1 \cos \phi)}{\delta(t_1)^{1/2}},\tag{A9}$$

$$x_0(t_1) = \mathsf{a}_1 \cos t_1 - \mathsf{a}_2 \cos t_2 \cos \phi + \mathsf{b}_2 \sin t_2 \sin \phi,$$
 (A10)

$$y_0(t_1) = b_1 \sin t_1 - b_2 \sin t_2 \cos \phi - a_2 \cos t_2 \sin \phi,$$
 (A11)

where

$$\delta(t_1) = \mathsf{a}_2^2(\mathsf{a}_1^2\sin^2 t_1 + \mathsf{b}_1^2\cos^2 t_1) + (\mathsf{b}_2^2 - \mathsf{a}_2^2)(\mathsf{b}_1\cos t_1\sin\phi - \mathsf{a}_1\sin t_1\cos\phi)^2$$

$$= \mathsf{b}_2^2(\mathsf{a}_1^2\sin^2 t_1 + \mathsf{b}_1^2\cos^2 t_1) - (\mathsf{b}_2^2 - \mathsf{a}_2^2)(\mathsf{a}_1\sin t_1\sin\phi + \mathsf{b}_1\cos t_1\cos\phi)^2, \tag{A12}$$

The excluded area $A(\phi)$ can be calculated as

$$A(\phi) = \frac{1}{2} \int_0^{2\pi} \left[y_0'(t_1) x_0(t_1) - y_0(t_1) x_0'(t_1) \right] dt_1, \tag{A13}$$

After some long calculations we arrive at the following relatively simple formula for this function:

$$A(\phi) = \pi(\mathsf{a}_1\mathsf{b}_1 + \mathsf{a}_2\mathsf{b}_2) + 2\left[\Delta_+(\phi) + \Delta_-(\phi)\right]E[\kappa(\phi)],\tag{A14}$$

where $E(\kappa) = \int_0^{\pi/2} \sqrt{1 - \kappa \sin^2 \theta} d\theta$ is the complete elliptic integral of the second kind and where we have defined

$$\kappa(\phi) = \frac{4\Delta_{+}(\phi)\Delta_{-}(\phi)}{\left[\Delta_{+}(\phi) + \Delta_{-}(\phi)\right]^{2}},\tag{A15}$$

$$\Delta_{\pm}(\phi) = \sqrt{(b_1 b_2 \pm a_1 a_2)^2 - (b_2^2 - a_2^2)(b_1^2 - a_1^2)\cos^2\phi}. \tag{A16}$$

Appendix B: Ellipse-rectangle excluded area

The purpose of this section is to obtain an expression for the excluded area between an ellipse with semi-axes a and b (b > a) and a rectangle with length and width equal to L and σ , respectively. We show in Figure 4 an schematic representation of the excluded area. It can be seen from the figure that the total area can be computed by summing two different contributions: (i) one coming from four triangles (two of them having different areas $A_i^{(t)}$,

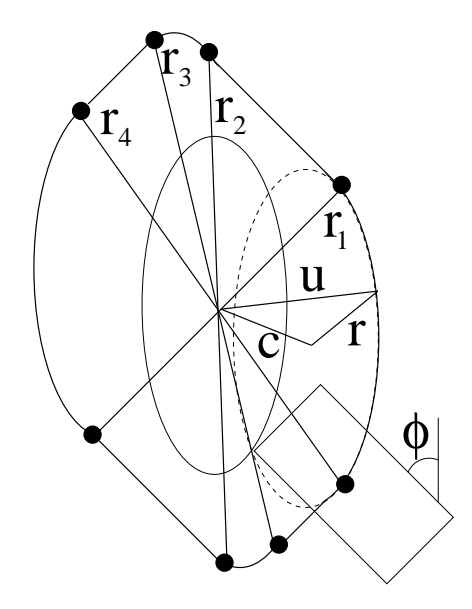


FIG. 10: The excluded area between an ellipse with semi-axes \mathbf{a} and \mathbf{b} and a rectangle of width σ and length L. Different sections of the excluded area are shown.

i = 1, 2) and (ii) the second, coming from four figures with elliptical borders (two of them having areas $A_i^{(e)}$, i = 1, 2). The areas corresponding to the triangles are

$$A_1^{(t)} = \frac{1}{4} \sqrt{4(r_1 r_2)^2 - (r_1^2 + r_2^2 - L^2)^2},$$
 (B1)

$$A_2^{(t)} = \frac{1}{4} \sqrt{4(r_3 r_4)^2 - (r_3^2 + r_4^2 - \sigma^2)^2},$$
 (B2)

where r_i are the absolute values of the vectors shown in Figure 4. These areas can be computed as

$$A_1^{(t)} = \frac{L}{2} \left[\frac{\sigma}{2} + \sqrt{\mathsf{a}^2 \cos^2 \phi + \mathsf{b}^2 \sin^2 \phi} \right],$$
 (B3)

$$A_2^{(t)} = \frac{\sigma}{2} \left[\frac{L}{2} + \sqrt{\mathsf{a}^2 \sin^2 \phi + \mathsf{b}^2 \cos^2 \phi} \right],$$
 (B4)

To compute the areas of figures with the elliptical borders we define the radius vector \mathbf{u} from the origin to the border of the excluded area (see Figure 10), which in turns is equal to the sum of two vectors: the vector $\mathbf{c} = (c_x, c_y)$ which accounts for the position of the center of mass of the rectangle with its inner vertex touching the perimeter of the ellipse and the vector $\mathbf{r} = (\mathbf{a}\cos\theta, \mathbf{b}\sin\theta)$ which has been parametrised with the angle $\theta \in [\theta_1, \theta_2]$. Thus, the area of this figure can be calculated from

$$A^{(e)} = \frac{1}{2} \int_{\psi_1}^{\psi_2} u^2(\psi) d\psi = \frac{1}{2} \int_{\theta_1}^{\theta_2} u^2(\theta) \psi'(\theta) d\theta,$$
 (B5)

with ψ the angle that the vector **u** forms with the x-axis. Taking into account the fact that $u = \sqrt{(a\cos\theta + c_x)^2 + (b\sin\theta + c_y)^2}$ and

$$\sin \psi = u^{-1} \left(c_y + \mathsf{b} \sin \theta \right), \quad \cos \psi = u^{-1} \left(c_x + \mathsf{a} \cos \theta \right), \tag{B6}$$

we find from (B5) that

$$A_i^{(e)} = \frac{1}{2} \left[\mathsf{ab} \left(\theta_2^{(i)} - \theta_1^{(i)} \right) + \mathsf{b} c_x \left(\sin \theta_2^{(i)} - \sin \theta_1^{(i)} \right) - \mathsf{a} c_y^{(i)} \left(\cos \theta_2^{(i)} - \cos \theta_1^{(i)} \right) \right], \tag{B7}$$

where $c_{x,y}^{(i)}$ are the components of the vector $\mathbf{c}^{(i)}$ describing the movement of the center of mass of the rectangle inside the two different regions with elliptical borders, while $\theta_{1,2}^{(i)}$ are the lower and upper limits of the parameter θ inside these regions. All these quantities are explicit functions of $\mathbf{a}, \mathbf{b}, \sigma$ and L. It can be easily shown that

$$\sum_{i} A_{i}^{(e)} = \frac{\pi}{2} \mathsf{a} \mathsf{b} + \frac{L}{2} \sqrt{\mathsf{a}^{2} \cos^{2} \phi + \mathsf{b}^{2} \sin^{2} \phi} + \frac{\sigma}{2} \sqrt{\mathsf{a}^{2} \sin^{2} \phi + \mathsf{b}^{2} \cos^{2} \phi}. \tag{B8}$$

Thus, the total excluded area can be obtained by summing all the contributions, i.e. $A(\phi) = 2\sum_{i} \left[A_{i}^{(t)} + A_{i}^{(e)} \right]$, with the final result

$$A(\phi) = L\sigma + \pi \mathsf{a}\mathsf{b} + 2\left[\sigma\sqrt{\mathsf{a}^2\sin^2\phi + \mathsf{b}^2\cos^2\phi} + L\sqrt{\mathsf{a}^2\cos^2\phi + \mathsf{b}^2\sin^2\phi}\right]. \tag{B9}$$

Appendix C: Minimization of the Gibbs free-energy per particle

As we have already pointed out before, the double angular average $\langle \langle A_{\mu\nu}^{(0)} \rangle \rangle$ is the main ingredient of SPT which can be computed as

$$\langle \langle A_{\mu\nu}^{(0)} \rangle \rangle = \int_0^{\pi} d\phi \Psi_{\mu\nu}(\phi) A_{\mu\nu}^{(0)}(\phi), \tag{C1}$$

where the functions

$$\Psi_{\mu\nu}(\phi) = \int_0^{\pi} d\phi' h_{\mu}(\phi') h_{\nu}(\phi + \phi'), \tag{C2}$$

were defined, which using Equation (4) become

$$\Psi_{\mu\nu}(\phi) = \frac{I_0[\xi_{\mu\nu}(\phi)]}{\pi I_0(\lambda_{\mu})I_0(\lambda_{\nu})},\tag{C3}$$

$$\xi_{\mu\nu}(\phi) = \sqrt{\lambda_{\mu}^2 + \lambda_{\nu}^2 + 2\lambda_{\mu}\lambda_{\nu}\cos 2\phi}.$$
 (C4)

To numerically implement the minimization of the Gibbs free energy per particle g with respect to the parameters λ_{μ} we have used the following expressions for the derivative of g with respect to λ_{μ}

$$\frac{\partial g}{\partial \lambda_{\mu}} = x_{\mu} \left\{ \lambda_{\mu} \left[1 - \frac{I_1^2(\lambda_{\mu})}{I_0^2(\lambda_{\mu})} \right] - \frac{I_1(\lambda_{\mu})}{I_0(\lambda_{\mu})} + y \sum_{\nu} x_{\nu} S_{\mu\nu} \right\}, \tag{C5}$$

$$S_{\mu\nu} = \int_0^{\pi} d\phi \frac{\partial \Psi_{\mu\nu}(\phi)}{\partial \lambda_{\mu}} A_{\mu\nu}^{(0)}(\phi), \tag{C6}$$

where

$$\frac{\partial \Psi_{\mu\nu}(\phi)}{\partial \lambda_{\mu}} = \frac{1}{\pi I_0(\lambda_{\nu}) I_0^2(\lambda_{\mu})} \left[(\lambda_{\mu} + \lambda_{\nu} \cos 2\phi) \frac{I_1(\xi_{\mu\nu})}{\xi_{\mu\nu}} I_0(\lambda_{\mu}) - I_0(\xi_{\mu\nu}) I_1(\lambda_{\mu}) \right]. \tag{C7}$$

We have solved the set of two non-linear equations $\partial g/\partial \lambda_{\mu} = 0 \ (\mu = 1, 2)$ with respect to two unknowns (λ_1, λ_2) .

- [1] van Roij, R.; Mulder B. J. Phys. II **1994**, 4 (10), 1763–1769.
- [2] Wensink, H.H.; Vroege, G.J.; Lekkerkerker, H.N.W. J. Chem. Phys. 2001, 115 (15), 7319–7329.
- [3] Dubois, S.; Perera, A. J. Chem. Phys. **2002**, 116 (14), 6354–6367.
- [4] Perera, A.; Cassou, K.; Ple, F.; Dubois, S. Mol. Phys. 2002, 100 (21), 3409–3419.
- [5] Varga, Sr.; Galindo, A.; Jackson, G. J. Chem. Phys. **2002**, 117 (15), 7207–7221.
- [6] Galindo, A.; Haslam, A.J.; Varga, S.; Jackson, G.; Vanakaras, A.G.; Photinos, D.J.; Dunmur, D.A. J. Chem. Phys. 2003, 119 (10), 5216–5225.
- [7] Martínez-Ratón, Y.; Cuesta, J.A. J. Chem. Phys. 2003, 118 (22), 10164–10173.
- [8] Schmidt, M.; Denton, A.R. Phys. Rev. E 2002, 65 (2), 021508.
- [9] Schmidt, M.; Denton, A.R. Phys. Rev. E 2002, 65 (6), 061410.
- [10] van Roij, R.; Mulder, B. Phys. Rev. E 1996, 54 (6), 6430–6440.
- [11] van Roij, R.; Mulder, B.; Dijkstra, M. Physica A 1998, 261 (3-4), 374–390.
- [12] Dijkstra, M.; van Roij, R. Phys. Rev. E 1997, 56 (5), 5594–5602.
- [13] Varga, S.; Galindo, A.; Jackson, G. Mol. Phys. 2003, 101 (6), 817–825.
- [14] Purdy, K. R.; Varga, S.; Galindo, A.; Jackson, G.; Fraden, S. Phys. Rev. Lett. 2005, 94 (5), 057801.

- [15] Onsager, L. Ann. N. Y. Acad. Sci. 1949, 51 (4), 627–659.
- [16] Parsons, J. D. Phys. Rev. A 1979, 19 (3), 1225–1230.
- [17] Reiss, H.; Frisch, H. L.; Lebowitz, J. L. J. Chem. Phys. 1959, 31 (2), 369–380.
- [18] Cotter, M.A.; Martire, D.E. J. Chem. Phys. 1970, 52 (4), 1902.
- [19] Cotter, M.A.; Martire, D.E. J. Chem. Phys. 1970, 53 (12), 4500.
- [20] Cotter, M.A.; Wacker, D.C. Phys. Rev. A 1978, 18 (6), 2669–2675.
- [21] Lasher, G. J. Chem. Phys. 1970, 53 (11), 4141.
- [22] Barboy, B.; Gelbart, W. J. Chem. Phys. 1979, 71 (7), 3053–3062.
- [23] P. Pieranski, Phys. Rev. Lett. 45, 569 (1980).
- [24] M. G. Basavaraj, G. G. Fuller, J. Fransaer, and J. Vermant, Langmuir 22, 6605 (2006).
- [25] J. de Graaf, M. Dijkstra and R. van Roij, J. Chem. Phys. 132, 164902 (2010).
- [26] Colloidal particles at liquid interfaces, B. P. Binks and T. S. Horosov (eds.), Cambridge University Press, Cambbridge 2006.
- [27] Aronson, I. S.; Tsimring, L.S. Rev. Mod. Phys. 2006, 78 (2), 641–692.
- [28] Galanis, J.; Harries, D.; Sackett, D.L.; Losert, W.; Nossal, R. Phys. Rev. Lett. 2006, 96 (2), 028002.
- [29] Narayan, V.; Menon, N.; Ramaswamy, S. J. Stat. Mech.: Theory Exp. 2006, P01005.
- [30] Talbot, J. J. Chem. Phys. **1997**, 106 (11), 4696–4706.
- [31] Martínez-Ratón, Y.; Velasco, E.; Mederos, L. Phys. Rev. E 2005, 72 (3), 031703.
- [32] de las Heras, D.; Martínez-Ratón, Y.; Velasco, E. Phys. Rev. E 2007, 76 (3), 031704.
- [33] Cuesta, J.A.; Frenkel, D. Phys. Rev. A 1990, 42 (4), 2126–2136.
- [34] Schlacken, H.; Mogel, H.-J.; Schiller, P. Mol. Phys. 1998, 93 (5), 777–787.
- [35] Zheng, X.; Palffy-Muhoray, P. Phys. Rev. E 2007, 75 (6), 061709.